

# The phase spiral in Gaia DR3

T. Antoja<sup>1,2,3</sup>, P. Ramos<sup>1,2,3,4</sup>, B. García-Conde<sup>5</sup>, M. Bernet<sup>1,2,3</sup>, C. F. P. Laporte<sup>1,2,3</sup>, and D. Katz<sup>6</sup>

<sup>1</sup> Departament de Física Quàntica i Astrofísica (FQA), Universitat de Barcelona (UB), c. Martí i Franquès, 1, 08028 Barcelona, Spain  
e-mail: tantoja@fqa.ub.edu

<sup>2</sup> Institut de Ciències del Cosmos (ICCUB), Universitat de Barcelona (UB), c. Martí i Franquès, 1, 08028 Barcelona, Spain

<sup>3</sup> Institut d'Estudis Espacials de Catalunya (IEEC), c. Gran Capità, 2-4, 08034 Barcelona, Spain

<sup>4</sup> (Research Affiliate) National Astronomical Observatory of Japan, Mitaka-shi, Tokyo 181-8588, Japan

<sup>5</sup> Departamento de Física de la Tierra y Astrofísica, Fac. CC. Físicas, Universidad Complutense de Madrid, Plaza de las Ciencias, 1, Madrid, E-28040, Spain

<sup>6</sup> GEPI, Observatoire de Paris, Université PSL, CNRS, 5 Place Jules Janssen, 92190 Meudon, France

Received November 21, 2022; accepted xxxxx

## ABSTRACT

**Aims.** We aim to study the phase spiral resulting from a phase mixing process in the Milky Way (MW) disc and use it as an inference tool to decipher the late time evolution of the Galaxy.

**Methods.** We analysed the phase spiral with data from *Gaia* DR3. We used an edge detection algorithm to find the border of the phase spiral, allowing us to robustly quantify its shape at different positions and for different selections. We calculated the time of onset of the phase-mixing by determining the different turns of the phase spiral and using the vertical frequencies from standard potential models of the MW.

**Results.** We find that the phase spiral extends down to  $-1.2$  kpc in height below the plane (about 3 to 5 scale heights of the thin disc) and beyond  $\pm 50$  km s<sup>-1</sup> in  $V_z$ . We see a secondary branch mostly at positive vertical velocities in the local phase spiral when coloured by azimuthal velocity, and also at different angular momentum in the counts projection. We also find complex variations of the phase spirals with angular momentum and azimuth. All these possibly provide evidence of multiple perturbations (from different times or from different perturbers) and/or that the disc is affected by complex phase mixing processes. We detect the phase spiral from 6 to 11 kpc and find signatures of vertical asymmetries 1-2 kpc beyond this range. We measure small but clear variations with azimuth. When we determine the phase mixing times from the phase spiral at different angular momenta and using the different spiral turns (at different  $Z$ ) we obtain inconsistent times with systematic differences (times increasing with  $|L_z|$  and with  $|Z|$ ). Our determinations are mostly in the range of [0.3-0.9] Gyr, with an average of 0.5 Gyr. The inconsistencies do not change when using different standard potential models for the MW, different stellar distances and frequencies for different kinetic temperatures. They could stem from the inconsistency of potential models with the true MW, and from too simple modelling, in particular neglecting self-gravity, not considering the multiple perturbations and the interference with other processes.

**Conclusions.** All these wealth of information provided by the new *Gaia* DR3 data should encourage us to progress on crucial modelling aspects of the disc dynamics such as non-equilibrium, self-gravity, propagation of different types of bending waves and interaction between different mechanisms.

**Key words.** Galaxy: kinematics and dynamics– Galaxy: evolution– Galaxy: disk – Galaxy: structure– Galaxies: interactions–

## 1. Introduction

The snail shell or phase spiral that appeared in the vertical projection of the phase space (Antoja et al. 2018, A18 hereafter) in the *Gaia* DR2 data (Gaia Collaboration et al. 2016, 2018) informed us about a process of phase mixing after certain perturbation from which the Milky Way (MW) is still recovering. This provided further details about the vertical asymmetries discovered by Widrow et al. (2012) and Williams et al. (2013).

Later we learned that the phase spiral shrinks in the  $Z$  direction when moving from the outer to the inner parts of the Galaxy (Laporte et al. 2019; Wang et al. 2019) as expected, that it is more prominent for cold orbits (Bland-Hawthorn et al. 2019; Li & Shen 2020), that it shows mild changes with azimuth (e.g. slightly different density of stars along the phase spiral, Bland-Hawthorn et al. 2019), and that it is present in different age ranges (Tian et al. 2018; Laporte et al. 2019; Bland-Hawthorn et al. 2019), even in samples younger than 0.5 Gyr. The fanning

of the phase spiral when colour-coded by the azimuthal velocity can be explained by the different vertical frequencies at different angular momentum (A18).

As for the causes of the phase spiral, most of the work favours the impact caused by the approaches of the Sagittarius dwarf galaxy (A18, Binney & Schönrich 2018; Laporte et al. 2018; Bland-Hawthorn & Tepper-García 2021). However, there are several complex aspects involved such as the effects of self-gravity discussed in Darling & Widrow (2019), the mass of Sagittarius needed to activate phase spirals (e.g. see discussions in García-Conde et al. 2022) or which could be the pericenter/s that excited them. Alternatively, it might have been caused by bending waves sparked by the buckling of the bar (Khoperskov et al. 2019) or the impact of several (dark) sub-halos (Chequers et al. 2018).

The shape of the phase spiral offers a way to constraint both the perturber and the potential of the Galaxy through the vertical orbital frequencies of the stars. In A18 we assumed a set of fre-

quencies of the MW and derived a perturbation time of 300-900 Myr. Ideally, both the potential and the perturbation times can be fitted at the same time as in Widmark et al. (2021), although these two quantities appear degenerated in the fit.

Aside of its inferring power, the phase spiral also alerted us that the assumption of a Galaxy in equilibrium may have biased determinations such as of the quantity of dark matter through the Jeans equations (Haines et al. 2019; Chrobáková et al. 2020). In addition, the vertical perturbations that led to the phase spiral might have other important consequences for the Galaxy. It might have come accompanied by disturbances in the other components of phase space and changes in the morphology of the MW (Laporte et al. 2018; Bland-Hawthorn & Tepper-García 2021; Antoja et al. 2022), as earlier proposed, for example, by Younger et al. (2008) and Purcell et al. (2011). The event might also be related to different episodes of strong star formation in the disc discovered with *Gaia* data as well (Mor et al. 2019; Ruiz-Lara et al. 2020).

The publication of *Gaia* DR3 (Gaia Collaboration et al. 2022c) offers now a new opportunity to explore the phase spiral across the disc and its stellar composition through the better selection of populations. For example, Gaia Collaboration et al. (2022b) showed that the phase spiral also appears when painted by metallicity due to the correlation between metallicity and angular momentum. Recently, Hunt et al. (2022) discovered double spirals in the inner parts of the Galaxy and they demonstrated that they could be due to breathing modes excited by internal structures such as the bar (but not necessarily a buckling bar) and also by an external perturber, similar to the double spirals from their simulations (Hunt et al. 2021).

Here we explore the phase spiral with *Gaia* DR3 data and try to do a new determination of the perturbation time. In Sect. 2 we describe the data selection and corrections. In Sect. 3 we explore the local phase spiral now with many more stars and better resolution (Sect. 3.1); we describe our method to detect the phase spiral and obtain its exact position in the  $Z$ - $V_Z$  plane (Sect. 3.2); and we further explore its spatial variations as a function of radius and angular momentum (Sect. 3.3 and 3.4) as well as azimuth (Sect. 3.5). In Sect. 4 we provide a fit to the time of perturbation similar to A18 but now considering the phase spiral at different angular momenta, which show interesting inconsistencies. In Sect. 5 we discuss our findings and conclude.

## 2. Data

We used data from *Gaia* DR3 (Gaia Collaboration et al. 2022c). We selected stars with available radial velocity and applied the following quality selections:

1. astrometric quality selection:

$$\text{RUWE} < 1.4, \quad (1)$$

2. selection in parallax quality:

$$\text{parallax\_over\_error} > 5, \quad (2)$$

3. selection of non-spurious solutions (Rybizki et al. 2022):

$$\text{fidelity\_v2} > 0.5. \quad (3)$$

We used by default distances from StarHorse (hereafter SH, Anders et al. 2022). We also used the photogeometric distances from Bailer-Jones et al. (2021, BJ hereafter) for comparison (finding no important differences in our results) and also to test the robustness of the detections (see Sect. 3.3).

In addition, we applied the following correction to the line-of-sight velocity for stars with  $\text{grvs\_mag} \geq 11$  and  $\text{rv\_template\_teff} < 8500$  (Katz et al. 2022):

$$\begin{aligned} \text{radial\_velocity} = & \text{radial\_velocity} \\ & -0.02755 * \text{grvs\_mag}^2 \\ & +0.55863 * \text{grvs\_mag} - 2.81129 \end{aligned} \quad (4)$$

As discussed in Blomme et al. (2022), a correction is also necessary for the stars with  $8500 \leq \text{rv\_template\_teff} \leq 14500$  K &  $6 \leq \text{grvs\_mag} \leq 12$  but after the correction there is still a residual bias of a few  $\text{km s}^{-1}$ . Since these stars are not very numerous, in our samples we keep only stars with  $\text{rv\_template\_teff} < 8500$  K.

After all the above selections, the final sample with SH distances has 25 397 569 stars, while the one with BJ distances contains 26 407 121 stars. The queries used to retrieve the data from the *Gaia* archive are presented in Appendix A. In Appendix B we compare the two sets of distances and in Appendixes C and D we discuss the effects of distances errors/biases and the selection function, respectively, on the detected phase spiral.

We transform the *Gaia* observables into usual cylindrical phase space coordinates. For this we use  $R_0 = 8.277$  kpc (Gravity Collaboration et al. 2022),  $Z_\odot = 0.0208$  kpc (Bennett & Boyv 2019), and  $U_\odot = 9.3$ ,  $V_\odot + V_c(R_0) = 251.5$  and  $W_\odot = 8.59$   $\text{km s}^{-1}$ , from the combination of the proper motion of SagA\* from Reid & Brunthaler 2020 and its radial velocity from Gravity Collaboration et al. (2022), where  $U, V, W$  are the usual heliocentric Cartesian velocities and  $v_c(R_0)$  as the circular velocity curve at the Sun's position. Our reference system is a right-handed one with  $\phi < 0$  in the sense of rotation, and thus also  $V_\phi < 0$  for most of the stars. We set the origin at the Sun's azimuth ( $\phi_\odot = 0$ ).

## 3. The phase spiral in DR3

### 3.1. The local phase spiral

In Fig. 1 we look at the local phase spiral in the  $Z$ - $V_Z$  plane by selecting stars with  $R_0 - 0.1$  kpc  $< R < R_0 + 0.1$  kpc and  $-20 < \phi < 20$  deg. This large range in  $\phi$  is justified by the phase spiral not changing much with  $\phi$  compared to  $R$ , as we see later on. In A18 with DR2 data, only the radial cut was performed, making a sample of 935 590 stars. Now we have a local sample with 2 328 004 stars. We note that we have increased the range in  $Z$  and  $V_Z$  of the panels in Fig. 1 compared to our previous work. We used bins with size  $\Delta Z = 0.02$  kpc and  $\Delta V_Z = 1$   $\text{km s}^{-1}$ . The three panels of Fig. 1 (counts and coloured by median  $V_R$  and by median  $V_\phi$ , respectively) show now a sharper signal. For example, the middle panel presents defined spiral segments of different  $V_R$ , including two blue segments in the upper left part. In the right panel the phase spiral has a secondary branch at  $50$   $\text{km s}^{-1}$ . While this could be partially observed in DR2 (A18, Laporte et al. 2019), now it emerges clearly separately from the other (main) spiral. This branching reaches now  $Z = -1.2$  kpc, thus about 3 to 5 scale heights of the thin disc (taken to be 220–450 pc, Bland-Hawthorn & Gerhard 2016, and references therein).

### 3.2. Detection of the phase spiral

In this section we describe the method that we used to detect and study the shape of the spiral. It is based on an edge-detector algorithm applied to the counts in the  $Z$ - $V_Z$  space. This technique takes the 2D histogram and reduces the noise using a Gaussian filter with a certain  $\sigma$  and, for each pixel (bin), calculates

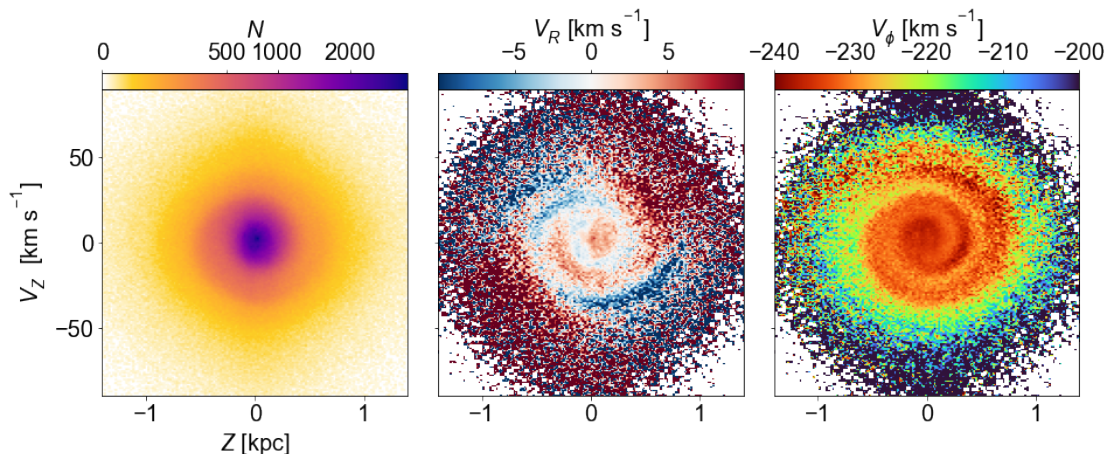


**Fig. 1.** Phase spiral in the solar neighbourhood with *Gaia* DR3 data. *Left*: Two-dimensional histogram of the vertical projection of phase space ( $Z-V_Z$ ) from the sample of stars with Galactocentric radii of  $R_\odot \pm 0.1$  kpc and  $\phi = 0 \pm 20$  deg. We used bins of  $\Delta Z = 0.02$  kpc and  $\Delta V_Z = 1$  km s $^{-1}$ . *Middle*: Same projection but colour-coded by median radial velocity  $V_R$ . *Right*: Same projection but colour-coded by median azimuthal velocity  $V_\phi$ , adjusting the colour bar limits so as to maximize the appearance of the spiral.

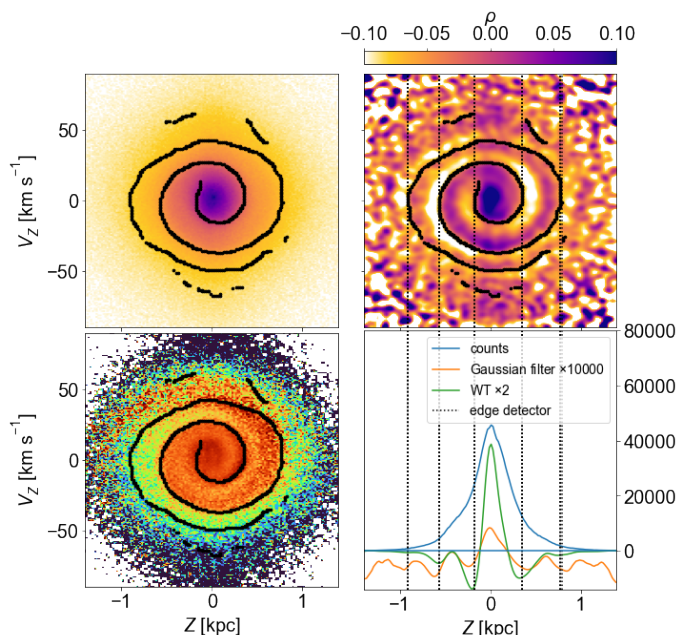


**Fig. 2.** Phase spiral detected by the edge detection. *Top left*: Output of the algorithm applied to the same selection of stars as in Fig. 1, superposed to the counts from which it has been computed. We used  $\sigma = 3$ . *Bottom left*: Same but superposed to the projection coloured by  $V_\phi$ . *Top right*: Comparison with the Gaussian filter (colour, see text). *Bottom right*: Comparison with the Gaussian filter and the WT, with the respective values scaled to fit in the same plot, as indicated in the legend, in a one-dimensional case (see text).

the gradients. Then the algorithm takes the pixels (bins) with the maximum gradients, which are always perpendicular to the edges, and further selects the edge bins by hysteresis thresholding. In most cases starting with a histogram on the logarithm of the number counts worked better (this is our standard option unless stated otherwise). We used the implementation in *python* `feature.canny` from *skimage* (van der Walt et al. 2014) which in practise returns a numerical matrix with 1's at the detected edges and 0 otherwise. We used a  $\sigma$  found empirically to provide good detections. For instance, for the solar neighbourhood

and binning defined in the previous section we used  $\sigma = 3$ . For volumes at smaller angular momentum  $|L_Z|$  explored in later sections, a larger  $\sigma$  worked better. In particular, we used  $\sigma=4.5$  for  $|L_Z| < 1600$  km s $^{-1}$ kpc and  $\sigma=3.5$  for  $|L_Z| \geq 1600$  km s $^{-1}$ kpc. The differences when using different  $\sigma$  are very small for most of cases, and, by construction, this will be within the error bars of the detections (Sect. 4). We note that this detector sometimes has problems in detecting the inner parts of the spiral. However, this is counterbalanced by the simplicity and speed of the algorithm and the good overall detection.

An illustration of the performance of the edge detector for the local phase spiral is shown in Fig. 2. In the top left panel we superpose the detected edge to the vertical phase space density. The edge detector perfectly delineates the main spiral and also finds signs of the upper branch in the local phase spiral. There is also a residual detection of an edge at  $V_Z \sim -70$  km s $^{-1}$  but with not so clear counterpart in the  $V_\phi$ -coloured projection. We note that the edge detector obtained from the counts projection approximately follows the spiral in the projection coloured by  $V_\phi$  (bottom left panel).

We have compared the results from the edge detector with previously used methods, namely the Gaussian filter and the Wavelet Transform (WT) (Antoja et al. 2015, and references therein). The former is similar to Laporte et al. (2019) but here we do  $\rho = H_2/H_4 - 1$ , where  $H_2$  and  $H_4$  are the original histogram of counts smoothed by a Gaussian filter (implementation `gaussian_filter` from *scipy*, Virtanen et al. 2020) with a  $\sigma_G = 2$  and  $\sigma_G = 4$  (in units of the pixel size,  $\Delta Z$  and  $\Delta V_Z$ ), respectively. For the WT we use the implementation `signal.cwt` from *scipy* with a width of the mother wavelet (Mexican hat) of 3 pixels. The top right panel compares the edge detector with the usual Gaussian filter while the bottom right panel compares the three methods for a one-dimensional projection with stars of  $|V_Z| < 3$  km s $^{-1}$ . The determinations from the three methods are very similar but the edge detector, by construction, manages better to detect the caustic edge that we are after.

### 3.3. The phase spiral with radius and angular momentum

In this section, we explore the spatial evolution of the phase spiral. First, in Fig. 3, we show the phase spiral coloured by median  $V_\phi$  for different Galactocentric radii, from inner (left) to outer

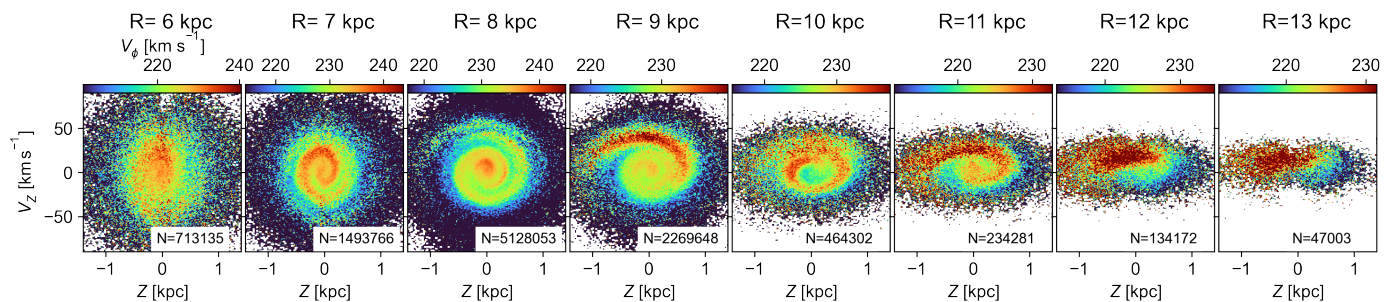


**Fig. 3.** Phase spiral at different Galactocentric radii with *Gaia* DR3 data. The panels show the vertical projection of phase space ( $Z$ – $V_Z$ ) coloured by median  $V_\phi$ . We only use stars with  $|\phi| < 20$  deg. The regions have a total radial width of 1 kpc and their centers are separated by the same amount. We used bins of  $\Delta Z = 0.02$  kpc and  $\Delta V_Z = 1$  km s $^{-1}$ . The colour-map ranges correspond to the percentiles 30 and 70 of the distribution of  $V_\phi$  in each volume to maximise the appearance of the spiral. In the bottom part of the panels we indicate the number of stars.

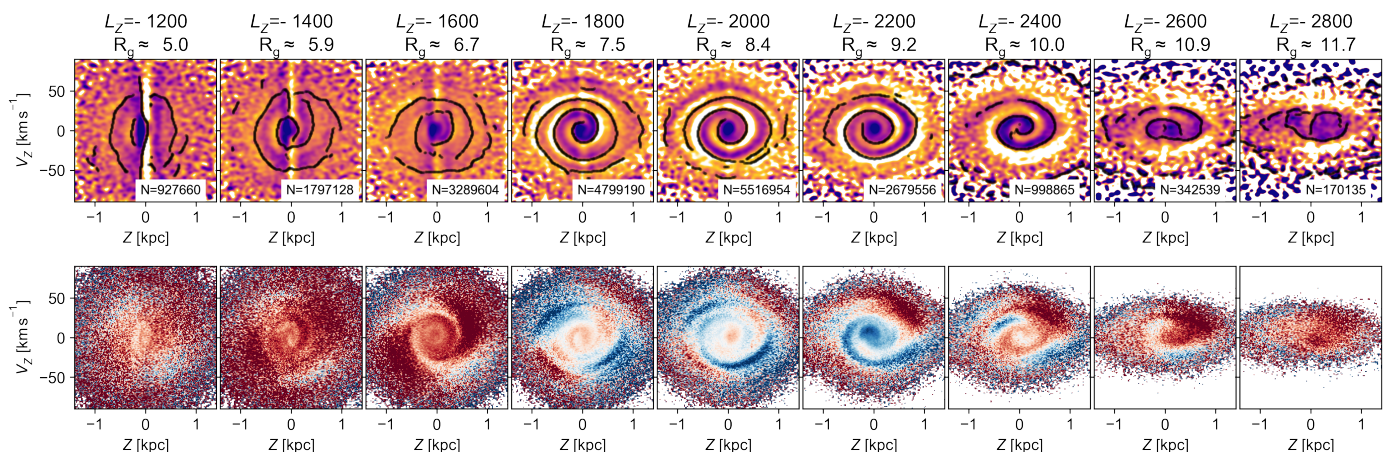


**Fig. 4.** Phase spiral for different angular momentum with *Gaia* DR3 data. We only use stars with  $|\phi| < 20$  deg. The selections have a total angular momentum width of 200 km s $^{-1}$ kpc and their centres are separated by the same amount. We used bins of  $\Delta Z = 0.02$  kpc and  $\Delta V_Z = 1$  km s $^{-1}$ . *Top*: Counts projection after Gaussian masking (see text for details). The colour bar is the same as in the top left panel of Fig. 2. We superpose our detected phase spiral via the edge detector method where we used  $\sigma=4.5$  for  $|L_Z| < 1600$  km s $^{-1}$ kpc and  $\sigma=3.5$  for  $|L_Z| \geq 1600$  km s $^{-1}$ kpc. We indicate the number of stars in the bottom part of the panels. *Bottom*: Projection coloured by  $V_R$  with the same colour-scale as in the central panel of Fig. 1.

radii (right), taking only stars with  $|\phi| < 20$  deg. The phase spiral becomes flatter with radius as already noticed before (e.g. Laporte et al. 2019; Bland-Hawthorn et al. 2019). With DR3 we see that the phase spiral is detected from 6 to 11 kpc, thus extending beyond the previous radial limits. In fact we also see hints of asymmetries reaching 5 and 13 kpc, possibly limited by the selection effects there.

We see a clear additional branching at  $V_Z \sim 50$  km s $^{-1}$  in the volume at  $R = 8$  kpc, which was already seen in Fig. 1, and now seems to extend slightly towards negative  $V_Z$  as well. From the animations with more continuous sweeping in  $R$  we see that this arch/branch shifts to lower  $V_Z$  with  $R$ , becoming mixed with the upper part of the main phase spiral and turning to an intense red ( $V_\phi$  lower than the local median). We also detect what seems to be another turn of the phase spiral or faint arch at  $V_Z \sim -50$  km s $^{-1}$  at the region of 7 kpc. Curiously, we also see a pattern with a “hole” close to the  $(Z, V_Z) = (0, 0)$  at 10 kpc (already noticed in *Gaia* DR2, e.g. Laporte et al. 2019).

Separating by  $L_Z$  instead of current radius yields a clearer spiral signal. This is because in this way we group stars with similar vertical frequencies (see the Extended Data Figure 4 in A18 and the corresponding explanation) and has been well demonstrated in Li (2021); Gandhi et al. (2022); Hunt et al. (2021). However, separating by angular momentum produces different

biases that are well explained for instance in Hunt et al. (2022), mostly the dominance of eccentric orbits at the extreme angular momentum of the sample.

In the top row of Fig. 4 we show phase spiral in counts for different bins of angular momentum. Again we only take stars with  $|\phi| < 20$  deg. In these panels an approximate measure of the guiding radius is given by simply doing  $R_g = L_Z/V_c(R_0)$ , assuming a flat circular velocity curve. The black lines show the results of the edge detector (see caption for details). For the last three panels (large angular momentum  $L_Z$ ) we applied the algorithm to the histogram of the counts (instead of the logarithm of the counts as in the other). This detects a better defined spiral for these cases but tends to detect a spiral biased towards inner parts. That is why we only use it for this figure but not when a quantitative comparison between panels needs to be done. In colours we plot the Gaussian filter as in the top right panel of Fig. 2. These panels show well defined phase spirals from  $R_g \sim 6$  to 11 kpc, and some hints of them beyond these. In the left panels, we see a vertical band empty of stars that is explained by the lack of stars at low  $|Z|$  towards the inner Galaxy due to extinction. The flattening of the spiral and their lower number of turns as one moves towards large  $|L_Z|$  is evident. We note that the double spiral at small angular momentum discovered by Hunt et al. (2022) is not seen here. This could be due to a main phase spiral dominating and

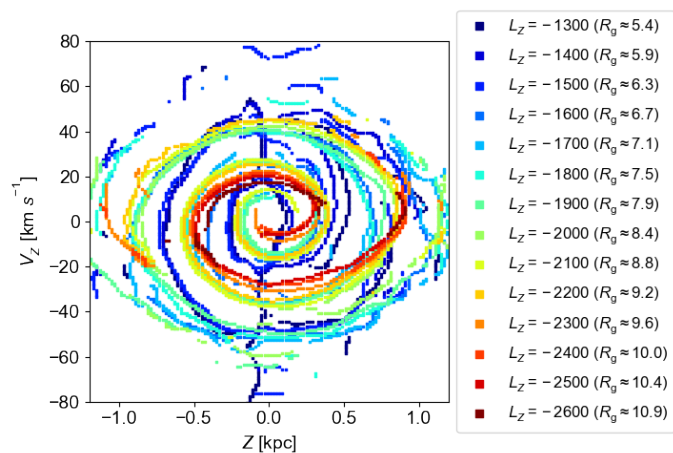


**Fig. 5.** Superposed phase spiral for different angular momentum with *Gaia* DR3 data. We select only stars with  $\phi \in [-20, 20]$  deg. We use bins of  $\Delta L_Z = 200 \text{ km s}^{-1} \text{ kpc}$  and centres of bins separated by  $100 \text{ km s}^{-1} \text{ kpc}$ , from  $L_Z = 1300 \text{ km s}^{-1} \text{ kpc}$  (bluer lines) to  $L_Z = 2500 \text{ km s}^{-1} \text{ kpc}$  (redder lines) as indicated in the legend. In parenthesis we give an indicative measure of guiding radius assuming a flat circular velocity curve.

masking the double branches here. Alternatively, it could be that, since Hunt et al. (2022) shows the phase spirals for a selection of nearby stars (1 kpc) split by angular momentum, the double spiral is only present for local stars with a small  $|L_Z|$ , that is when they are observed towards their apocentres. The upper separated branching seen at  $R \sim 8 \text{ kpc}$  can be seen in the Gaussian filter from  $R_g \sim 7.5$  to  $10 \text{ kpc}$  ( $|L_Z|$  from  $1800$  to  $2400 \text{ km s}^{-1} \text{ kpc}$ ). In some cases, for example at  $|L_Z| = 2200 \text{ km s}^{-1} \text{ kpc}$ , further turns at larger  $|Z|$  and  $|V_Z|$  can be seen in the background colours.

In the bottom row of Fig. 4 we colour coded the vertical phase space by median  $V_R$ . A trend of the global  $V_R$  with  $L_Z$  is noticeable with redder colours (positive  $V_R$ ) for small  $|L_Z|$ , bluer (negative  $V_R$ ) for intermediate  $|L_Z|$ , and again redder for large  $|L_Z|$ . This is related to the  $V_R$ - $L_Z$  waved detected in Friske & Schönrich (2019) (see also Antoja et al. 2022, and middle panel of the fourth row in Fig. D.1). We also see a quadrupole at the outer parts of these diagrams that is explained by the tilt of the velocity ellipsoid (Bland-Hawthorn et al. 2019). Aside from these, the phase spiral segments appear clear and sharp. We notice that the correspondence between density phase spiral and coloured by  $V_R$  is not univocal. For example, the blue  $V_R$  branch of the phase spiral at  $L_Z = -2200 \text{ km s}^{-1} \text{ kpc}$  extends to  $Z = 1.4 \text{ kpc}$  while the spiral segment in density continues to curl upwards. In some cases, we see that  $V_R$  changes sign along the spiral segments ( $L_Z = -2000 \text{ km s}^{-1} \text{ kpc}$ ).

In Fig. 5 we superpose the phase spirals detected by our algorithm (Sect. 3.2) for different values of  $L_Z$  as indicated in the legend, supplemented by their corresponding guiding radii  $R_g$  assuming a flat circular velocity curve, selecting only stars at the azimuth of the Sun with  $|\phi| < 20$  deg. An animated version of the plot will be made available online. We see an approximately continuous evolution of the phase spiral with angular momentum. The pitch angle increases as a function of  $L_Z$  (or  $R$ , as already mentioned), as expected. The dark blue curves show some vertical lines related to the selection effects explained above. We note that for the same incremental value in  $L_Z$  we do not see the same amount of morphological change, that is for some angular momentum the phase spiral changes more abruptly than for others (e.g. from dark to light blue).

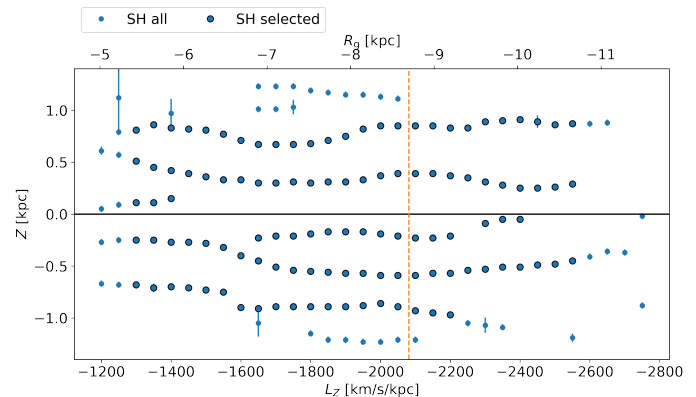


**Fig. 6.** Crossing positions of the phase spiral ( $Z_c$ ). The blue circles and error bars mark the  $Z$  coordinate for  $V_Z = 0$  of the phase spiral determined from the edge detector for the SH sample. We mark the positions used for inferring the impact time with empty black circles. The dashed orange vertical line marks the angular momentum of the Sun.

### 3.4. Crossing points of the phase spirals with $L_Z$

For the analysis of Sect. 4 we need the  $Z$  coordinate of the phase spiral when crossing the  $V_Z = 0$  line, which we call  $Z_c$ . We determined these crossings using our edge detection algorithm applied to the  $Z$ - $V_Z$  counts for different selections of angular momentum. We now use samples centred every  $50 \text{ km s}^{-1} \text{ kpc}$  (thus, with more continuity) with a total width of  $\Delta L_Z = 100 \text{ km s}^{-1} \text{ kpc}$  (thus, with some overlap and smaller than before to minimize variations of  $L_Z$  within a bin). We considered only stars with  $|\phi| < 20$  deg. Figure 6 shows  $Z_c$  as a function of  $L_Z$ . In blue we show all the  $Z_c$  from the edge detector, which show many continuous sequences corresponding to crossings that are well detected across several  $L_Z$  but also noisy/spurious detections at the extreme  $L_Z$ , where data is less numerous and distance errors are larger.

Formally, we would assign an error to each  $Z_c$  of the order of the bin size of the histogram in the  $Z$  coordinate to which the edge detector is applied, that is  $0.02 \text{ kpc}$ . However, we see that using a slightly different  $\sigma$  in the edge detector (from 2 to 5) may produce (in few cases) differences that are around  $0.03 \text{ kpc}$ . We thus take this as our baseline error. We also repeated the measurement of the  $Z_c$  with the BJ distances, computed the difference  $\delta Z = |Z_{c(\text{SH})} - Z_{c(\text{BJ})}|$  between the crossings from SH and BJ (considering the closest points) and to each  $Z_c$  from SH we arbitrarily assign an error of  $\text{MAX}(0.03 \text{ kpc}, \delta Z)$ . Also, for the final analysis we only considered  $Z_c$  with errors smaller than  $0.1 \text{ kpc}$  (i.e. not considering points in SH that differ from BJ more than  $0.1 \text{ kpc}$ ). The comparison between the detections with SH and BJ is shown in Fig. B.1. The differences are in general very small as expected from the small differences in distances at the ranges that we are probing (Appendix B). We also selected only points with  $|Z| < 1 \text{ kpc}$  since beyond this height the detections are also noisy and in some cases we are not certain that they really correspond to a crossing of the phase spiral or to some edge of the global distribution. We only took points with  $L_Z \in [-2600, -1300] \text{ km s}^{-1} \text{ kpc}$  as beyond these limits the phase spiral is not clear (Fig. 4).

In Fig. 6 the points that we consider valid after all the filters from above are circled in black. At angular momentum where there are more stars (mostly left to the Sun's one marked with a vertical dashed orange line), more turns are detected (3 for  $Z < 0$  compared to 2 at larger and smaller angular momentum), which is likely a combination of the selection effects and true differ-

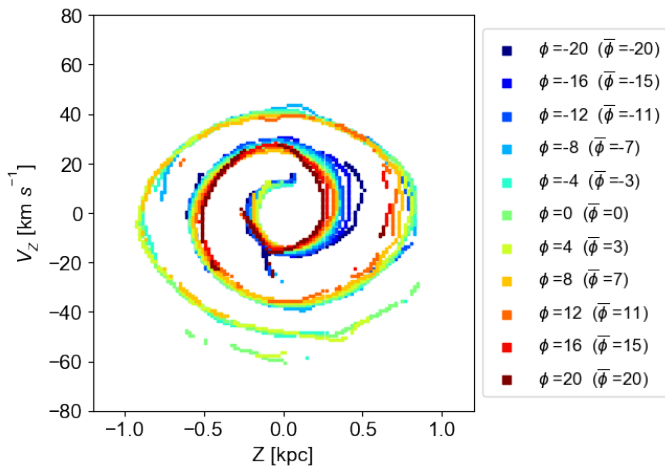


**Fig. 7.** Superposed phase spiral for different azimuths with *Gaia* DR3 data. We select only stars with  $L_Z \in [-2100, -1800]$ . We use bins of  $\Delta\phi = 4$  deg and centres of bins separated by the same amount, from  $\phi = -20$  deg (bluer lines) to  $\phi = 20$  deg (redder lines) as indicated in the legend. In parenthesis we give the average azimuth of the selection, which can differ by 1 deg compared to the center of the selection in some cases. For the edge detector we used  $\sigma = 3.5$ .

ences in the phase spiral (smaller pitch angle for larger  $|L_Z|$ ). We also see some abrupt jumps such as at  $L_Z \sim -1600 \text{ km s}^{-1} \text{ kpc}$  in the lowest turn ( $Z_c \approx -0.8 \text{ kpc}$ ). The influence of the selection function on the determinations of  $Z_c$  is analysed in Appendix D, where we conclude that some of these jumps could be due to slight changes in the dominating population at each  $L_Z$ . Aside from these jumps, the sequences of  $Z_c$  show undulations. These are not expected from a simple interpretation of the phase spiral in which we would see a continuous increase of  $|Z_c|$  towards the outer parts of the Galaxy (large  $|L_Z|$ ). This is because in usual Galaxy potential models the gradient of vertical frequencies with vertical amplitude is smaller in the outer parts of the Galaxy (Extended Data Fig. 4 in A18), leading to a less tightly wound phase spiral. This will have important implications in the phase mixing times that we derive from these measurements in Sect. 4.

### 3.5. The phase spiral with azimuth

In Fig. 7 we show the azimuthal variations of the phase spiral at fixed angular momentum. We choose  $L_Z \in [-2100, -1800] \text{ km s}^{-1} \text{ kpc}$  since this is the range around the value of  $L_Z$  with maximum density in our sample. We see less changes with  $\phi$  than with  $L_Z$  but there is a clear gradual change. In some parts of the phase spiral there is a larger variation with azimuth (e.g. turn at  $Z \sim 0.4$ ) than in other turns (e.g. turn at  $-0.5 \text{ kpc}$ ). To be more quantitative, for the crossings  $Z_c$  at  $V_Z = 0$  we measure a slope with  $\phi$  of  $-0.006$ ,  $-0.004$  and  $0.002 \text{ kpc/deg}$  for the crossings at  $0.8$ ,  $0.3$  and  $-0.6$ , respectively. The turns at  $Z \sim -0.2$  and  $Z \sim -0.9$  remain nearly constant with azimuth. A simple phase difference with  $\phi$  would produce the same level of fanning for each turn. Therefore, our observations require having an extra deformation (e.g. different level of winding-up at different azimuth, i.e. different phase spiral pitch angle) and/or having strong population differences with positive/negative  $Z$ . Finally, we see that the lowest turn of the spiral at  $V_Z \sim -50 \text{ km s}^{-1}$  is only seen in the azimuths close to the Sun likely due to having more stars in these volumes.

## 4. Inferring the impact time

### 4.1. Method

In a phase mixing process, the phase spiral gets more tightly wound with time and we can 're-wind' it to infer the onset time of the phase-mixing process which can then be linked to the time of the perturbation that originated it. In A18 we used the consecutive turning points of the local phase spiral to constrain the impact time assuming a model of the MW potential from which the vertical frequencies were derived empirically. Here we repeat the process of A18 but using data of the phase spiral at different angular momenta, helped by the increase of data at different positions across the Galaxy with the new *Gaia* DR3. Ideally, one could fit simultaneously the potential and time of the perturbation in the line of Widmark et al. (2021). This is, however, a degenerated problem and is not so straightforward after the findings of this work. Therefore, it will be a subject of a future study.

For this analysis we use the crossings  $Z_c$  of the phase spiral at  $V_Z = 0$  from the previous section (Fig. 3.3). Stars that have  $V_Z = 0$ , such as in these crossing points, are currently in their maximum vertical height (above or below the plane):  $Z = Z_{\text{max}}$ . Therefore, we can estimate the vertical frequencies of these points by interpolating into a grid of frequencies computed as a function of  $L_Z$  (or  $R_g$ ) and  $Z_{\text{max}}$ . Then each pair of consecutive crossings ( $Z_{c_1}, Z_{c_2}$ ) are separated by a phase  $2\pi$  and, thus, we can infer the impact time by their difference of vertical frequencies:

$$T = \frac{2\pi}{\nu(L_Z, Z_{c_1}) - \nu(L_Z, Z_{c_2})}. \quad (5)$$

Assuming that a single perturbation caused the phase spiral across the disc, this simple analysis should yield the same perturbation time at all  $L_Z$  and for each pair of crossings. We note that with DR3 we are able to use more pairs of crossings (two in the  $Z < 0$  part of the spiral and one in the  $Z > 0$  part) at angular momentum closer to the Sun's one, while in A18 we could only use two pairs in total. In A18 we used the crossings detected in the vertical phase space coloured by  $V_\phi$  and here we use the crossings from the edge detector on the counts.

To build the grid of frequencies we used *AGAMA* (Vasiliev 2019) and simulated more than 8,000 orbits at  $Z \geq 0$  (and use the vertical symmetry of the potential for the  $Z < 0$  part) in the McMillan (2017) potential (McM2017). The orbits were integrated for about 50 revolutions. They all started with null  $V_Z$  (i.e. at the top of their vertical oscillation). The other components of the initial conditions were set as follow:  $\phi = 0^\circ$ ,  $V_R = 0 \text{ km s}^{-1}$  (but see below for orbits with non-null radial action). Then we run through  $Z$  (from  $-4 \text{ kpc}$  to  $4 \text{ kpc}$  every  $50 \text{ pc}$ ) and  $L_z$  (from  $500 \text{ km s}^{-1} \text{ kpc}$  to  $3000 \text{ km s}^{-1} \text{ kpc}$  every  $25 \text{ km s}^{-1} \text{ kpc}$ ), solving numerically the implicit equation

$$L_z - \sqrt{-\frac{\partial\Phi(R, Z)}{\partial R}} R^3 = 0. \quad (6)$$

to obtain the  $R$ , and thus  $V_\phi = L_z/R$ , of the corresponding circular orbit. Subsequently, we sample each orbit with 20,000 points<sup>1</sup>

<sup>1</sup> We have tested the sensitivity of the measured frequency to both the number of samples used and the number of revolutions, finding a negligible dependence on the former (as long as there are more than a few hundred points) and an asymptotic behaviour as a function of the latter. For 50 revolutions, the error on the measured frequency tends to be of the order of less than 1%.

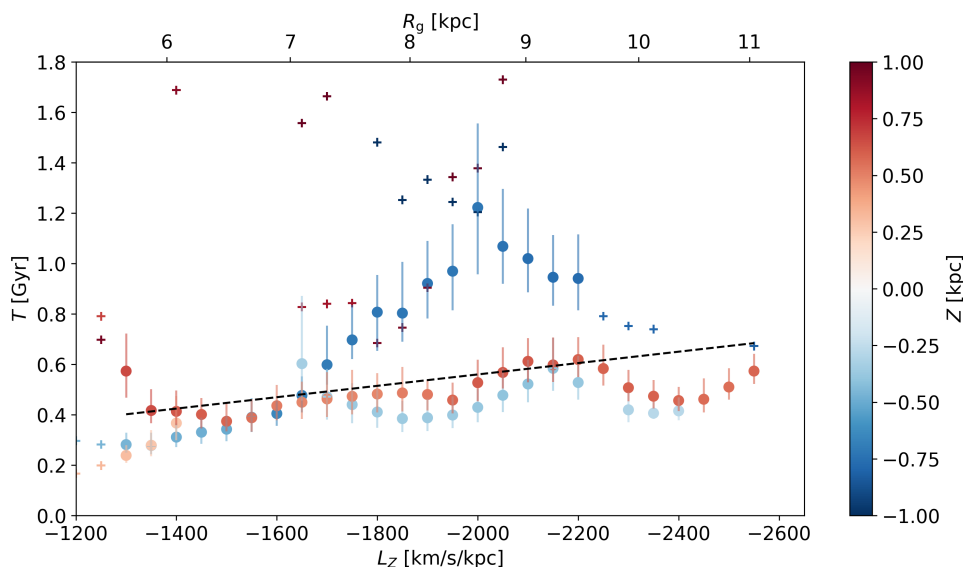


**Fig. 8.** Time of start of phase mixing as a function of angular momentum. The symbols give the time inferred from Eq. 5 for the different consecutive crossing points of the phase spiral and are coloured by height above the plane. The circles with error bars are the points that we consider valid while crosses are the rest of cases. An indicative guiding radius corresponding to the circular velocity curve of the McM17 potential is given in the upper horizontal axis. The dashed line marks a linear fit to the data points.

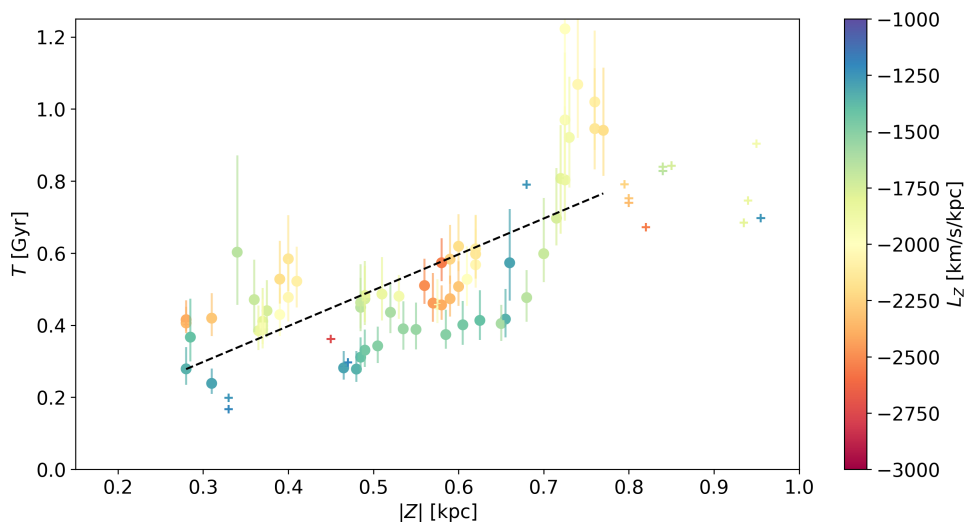


**Fig. 9.** Time of start of phase mixing as a function of height above the plane. The symbols give the time inferred from Eq. 5 for the different consecutive crossing points of the phase spiral and are coloured by angular momentum. The circles with error bars are the points that we consider valid while crosses are the rest of cases. The dashed line marks a linear fit to the data points.

and measure the vertical frequency with a Fast Fourier Transformation (Cooley & Tukey 1965) of the signal in  $Z$  as a function of time. Below we explore other potential models and frequencies for different kinetic temperatures.

#### 4.2. Time results

Interpolating in the above mentioned grid of frequencies and using Eq. 5, we infer the time of start of the phase obtained from each pair of crossings  $Z_c$ . In Fig. 8 we show the results as a function of  $L_z$  (horizontal axis) and  $Z$  (colour scale), where for the plot, we used the average  $(Z_{c_1} + Z_{c_2})/2$  of the points of the pair. With small + signs we have marked the time determinations from the  $Z_c$  that we do not consider valid (see text in Sect. 3.3, small blue circles in Fig. 6). These appear randomly scattered

around the plot (many of these points are outside the vertical range). Instead, circles with error bars are the ones from the valid  $Z_c$  after the considerations of Sect. 3.3. The error bars<sup>2</sup> are not symmetric because of the dependency of the frequencies with  $Z$ .

The valid times in Fig. 8 (error bars) show different coherent sequences. The sequences from small  $|Z_c|$  (both positive and negative, lighter colours) are distributed around 0.5 Gyr and in many cases are consistent within the errors at a fixed  $L_z$ . However, these points show increasing estimated times with  $|L_z|$ .

<sup>2</sup> To compute the upper (lower) limit in each derived time we used the limits of the errors of  $Z_c$  that minimize (maximize) the frequency difference. That is, for pairs of crossings with  $Z > 0$ , we considered the lower limit of the smaller  $Z_c$  and the upper limit of the larger  $Z_c$  to obtain the lower limit of the time (maximum vertical frequency difference). Conversely, the upper limit of time is obtained by combining the upper limit of the smaller  $Z_c$  and the lower limit of the larger  $Z_c$ .

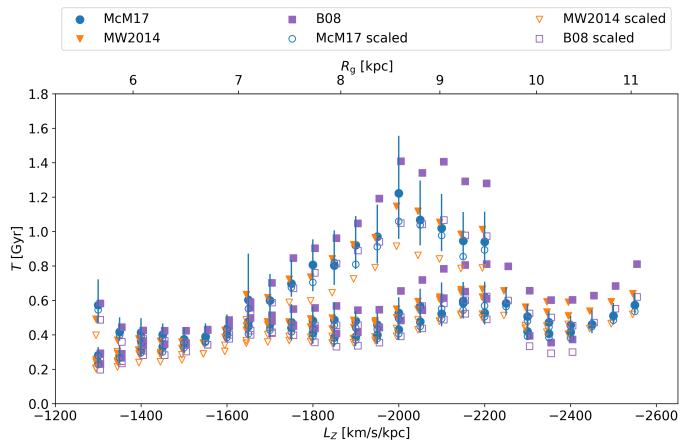


**Fig. 10.** Time of start of phase mixing for different potentials. The figure is similar to Fig. 8 but we use frequencies of different potential models of the MW, as indicated in the legend.

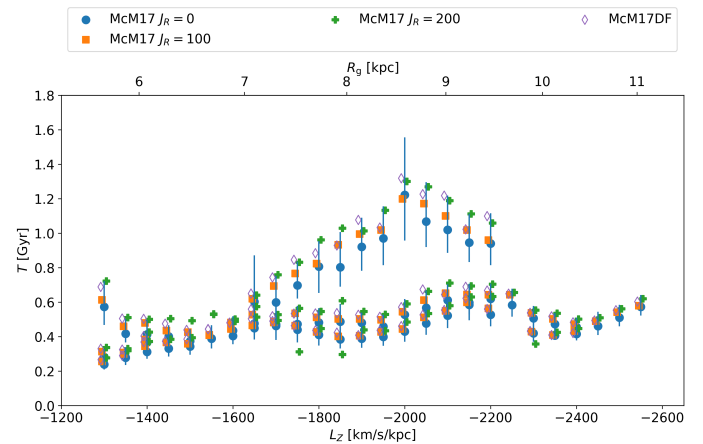
In addition, the darker blue points corresponding to the second crossing at  $Z < 0$  are at significantly larger times and show also a tendency to increase with angular momentum. A linear fit with  $L_Z$  to all the valid times gives  $T = (-0.00023 \pm 0.00007 \text{Gyr}(\text{km s}^{-1} \text{kpc})^{-1})L_Z + 0.011 \pm 0.14 \text{Gyr}$  (dashed line in Fig. 8). However, we see several oscillations in the different sequences, some of them corresponding to the oscillations in the  $Z_c$  (Fig. 6) already mentioned. This is examined further in Appendix D, where we conclude that while some oscillations could be related to changes in the dominating populations, the global trends with  $L_Z$  and  $Z$  might require a different explanation that we discuss in Sect. 5.

Fig. 9 is equivalent to Fig. 8 but as a function of  $|Z|$  (horizontal axis) and  $L_Z$  (colour scale). A general trend of time increasing with  $|Z|$  is observed. The linear fit gives  $T = (1.0 \pm 0.1 \text{Gyr}(\text{kpc})^{-1})|Z| - 0.0005 \pm 0.0800 \text{Gyr}$  (dashed line in Fig. 9), but this fit would depend on the angular momentum (colours in Fig. 9).

Ignoring for now the trend with  $Z$  and  $L_Z$  (which we discuss in Sect. 5), with an error-weighted average ( $w = 1/\sigma^2$ ) of all points we obtain a start of phase mixing time of 0.4 Gyr. We find that 80% of the time determinations are within  $[0.3, 0.9] \text{Gyr}$ . The variations with  $L_Z$  and  $Z$  are larger than the statistical error (error bars). In Table 1 (first row) we give also other statistics such as the unweighted average, and minimum and maximum values.

#### 4.3. Results for different models and data

We examined the dependency of the results on different different potential models (Fig. 10), frequencies for different kinetic temperatures (Fig. 11), and possible systematics in distance (Fig. 12). In all these figures blue circles show our standard model. The time statistics are given in Table 1, where the last two columns indicate the differences between the times of these new cases and the times from the standard model ( $T_0$ ). In most cases, the times are within the error bars of the standard case. We find the largest differences when we change the assumed potential model for the MW. In particular, we obtain systematically larger times for Model I (here B08) from Binney & Tremaine (2008) (on average 0.09 Gyr larger), and systematically smaller times for the MWpotential2014 (here MW2014) from Bovy (2015) when scaled to fit the values of  $V_c$  and  $R_0$  used in the data (on av-



**Fig. 11.** Time of start of phase mixing for different kinetic temperatures. The figure is similar to Fig. 8 but we use orbits with different radial actions and methods, as indicated in the legend.

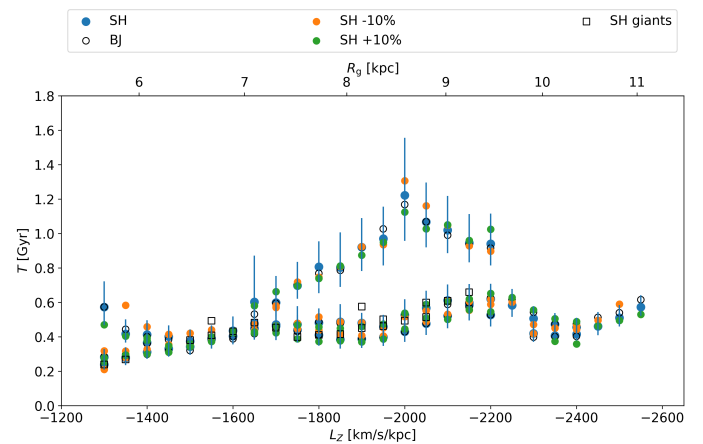


**Fig. 12.** Time of start of phase mixing for different distances and data. The figure is similar to Fig. 8 but we use distances from BJ, from SH with distance biases of  $\pm 10\%$  and for a selection of giant stars, as indicated in the legend.

erage 0.09 Gyr smaller). We also obtained systematically larger times when using not-circular orbits: for example 0.08 Gyr larger times for orbits with radial action  $J_R = 200 \text{km s}^{-1} \text{kpc}$ .

However, the main trends in the time determinations (in angular momentum and in height) remain the same in all cases. Our conclusions, thus, will be applicable to all the sets examined. Below we give details of this analysis but for a quick reading one could jump directly to the conclusions.

We first explored different potential models (Fig. 10), whose circular velocity curves are compared in Fig. E.1. These different potentials have different vertical frequencies as a function of radius and height, and thus, yield different time determinations.

- Orange triangles in Fig. 10 use MWpotential2014 (here MW2014) from Bovy (2015). This model returns slightly smaller times at smaller  $|L_Z|$  and larger times at larger  $|L_Z|$  but with null average differences when taking all individual time measurements. Purple squares are for the model Model I (here B08) from Binney & Tremaine (2008). With this case we obtain the largest differences from all the variations explored in this section, systematically larger than our standard case and with several points at  $2\sigma$ . The average differences are of 0.09 Gyr and 80% of time measurements are within  $[0.4, 1.] \text{Gyr}$ .

**Table 1.** Phase mixing times from the phase spirals. We show weighted and unweighted average (columns 2 and 3) with their standard errors, minimum and maximum values (columns 4 and 5), and ranges enclosing 80% of times (column 6). The last two columns (7 and 8) compare the times with the standard case (first row), showing the average differences and the ranges of differences. The different rows are for different cases as explained in the text.

Model	mean( $T$ )	weighted mean( $T$ )	min( $T$ )	max $T$	[P10, P90] $_T$	mean( $T - T_0$ )	[P10, P90] $_{T-T_0}$
McM17 $J_R = 0$	$0.5 \pm 0.03$	$0.4 \pm 0.01$	0.2	1.2	[0.3, 0.9]	0.00	[0.00, 0.00]
MW2014	$0.6 \pm 0.03$	$0.4 \pm 0.01$	0.2	1.1	[0.3, 0.9]	0.02	[-0.04, 0.08]
B08	$0.6 \pm 0.04$	$0.5 \pm 0.01$	0.2	1.4	[0.4, 1.0]	0.09	[-0.00, 0.21]
McM17 scaled	$0.5 \pm 0.02$	$0.4 \pm 0.01$	0.2	1.1	[0.3, 0.8]	-0.03	[-0.05, -0.01]
MW2014 scaled	$0.4 \pm 0.02$	$0.3 \pm 0.01$	0.2	0.9	[0.3, 0.7]	-0.09	[-0.17, -0.03]
B08 scaled	$0.5 \pm 0.03$	$0.4 \pm 0.01$	0.2	1.1	[0.3, 0.9]	-0.03	[-0.06, 0.02]
McM17 $J_R = 100$	$0.6 \pm 0.03$	$0.5 \pm 0.01$	0.3	1.2	[0.4, 1.0]	0.03	[0.01, 0.07]
McM17 $J_R = 200$	$0.6 \pm 0.03$	$0.5 \pm 0.01$	0.3	1.3	[0.4, 1.0]	0.08	[0.04, 0.15]
McM17 DF	$0.6 \pm 0.03$	$0.5 \pm 0.01$	0.3	1.3	[0.4, 1.0]	0.06	[0.02, 0.12]
$d_{SH-10\%}$	$0.5 \pm 0.03$	$0.4 \pm 0.01$	0.2	1.3	[0.4, 0.9]	0.02	[-0.03, 0.05]
$d_{SH+10\%}$	$0.5 \pm 0.03$	$0.4 \pm 0.01$	0.3	1.1	[0.3, 0.9]	-0.01	[-0.05, 0.03]
$d_{BJ}$	$0.5 \pm 0.03$	$0.4 \pm 0.01$	0.2	1.2	[0.3, 0.9]	-0.00	[-0.03, 0.03]
SH giants	$0.5 \pm 0.02$	$0.4 \pm 0.02$	0.2	0.7	[0.4, 0.6]	0.04	[-0.02, 0.10]

- While in the item above we use the original potential models from the respective articles, we also used them scaled to fit the values of  $V_c$  and  $R_0$  used in the data. To do this we use the built-in scaling mechanism of **AGAMA** by providing a mass scaling factor  $(V_c(R_0)_{\text{desired}}/V_c(R_0)_{\text{default}})^2$  at the time of creating the gravitational potential, which results in the velocities and frequencies being scaled as the square root of said scaling factor. The results for the scaled potentials are the empty symbols in Fig. 10. It is now the MW2014 (scaled) model that gives maximum differences with the standard case, yielding smaller times ([0.3, 0.7] Gyr).

Secondly, we examined different orbital conditions (Fig. 11), using frequencies for different kinetic temperatures. In our standard case we use orbits with  $J_R = 0$ , that is nearly circular orbits. Here we increase the eccentricity of the orbits in two different ways and use the corresponding new frequencies:

- Frequencies for orbits with larger radial actions ( $J_R = 100$  &  $J_R = 200$  km s<sup>-1</sup>kpc, orange squares and green crosses in Fig. 11). These cases yield in general larger times since hotter orbits have smaller differences between frequencies at different heights. The average time, though, does not change much.
- Frequencies for the most populated part of the distribution function (DF, purple diamonds in Fig. 11). This is done by fixing  $R$  and  $Z$  and estimating the vertical frequency of the orbit with the highest probability in the DF at that location of space, that is at  $Z_{\text{max}}$  ( $V_Z = 0$ ). With these different frequencies we obtain also larger times, similar to the  $J_R = 200$  case.

Finally, we compare our results with the ones using another set of distances, possible distance biases and a selection of giant stars (Fig. 12). This is also examined in Appendix C.

- Using the BJ distances our results barely change (empty black circles in Fig. 12). This is not surprising given the agreement between both sets of distances for our selected samples.
- Distance bias. If we decrease/increase the distances by 10% (orange and green circles in Fig. B.2), mimicking a correction of overestimated/underestimated distances, there is an increase/decrease in the value of  $|Z_c|$  approximately by the same amount (Appendix C, Eq. C.3), except at the extreme

$L_Z$  where selection effects might be playing a role. However, since Eq. 5 uses differential frequencies, we see that the times obtained do not change significantly (orange and green triangles in Fig. 12, consistent with the non-biased SH distances within the errors in most cases).

- Sample of giant stars. We also redid our analysis using the selection of giant stars from Gaia Collaboration et al. (2022a) obtained from the parameters of the *Gaia* `gspphot` pipeline with also the same quality filters as for our main sample. The new  $Z_c$  and derived times are shown in Fig. B.2 and Fig. 12 (empty black squares in both figures), respectively. In almost all cases the new values fall within the error bars of the standard case and the trend in angular momentum remains the same. We cannot check whether the times also increase with  $|Z|$  since only the inner parts of the spiral are detected due to the small number of stars in this selection (4 901 270).

## 5. Summary, discussion and conclusions

We have examined the phase spirals with the new data from *Gaia* DR3 and we find:

- A clear increase in the  $Z$  and  $V_Z$  ranges in which the phase spiral is detected. Surprisingly, we see phase spiral extending down to  $-1.2$  kpc, thus well into the realm of the thick disc. This does not necessarily mean that it is made of thick disc stars but could be made of thin disc stars that have been largely displaced.
- Phase spiral turns that extend in  $V_Z$  beyond  $\pm 50$  km s<sup>-1</sup>, meaning that the perturbation produced a velocity kick at least of this amount and/or affected stars with these high vertical velocities.
- An increase in the range of detection of phase spiral in Galactic radius and azimuth. We see clear phase spirals between 6 and 11 kpc in radius and also evident asymmetry, probably indicative of a poorly resolved spiral, down to 5 kpc and up to 13 kpc (Fig. 3).
- Clearer phase spirals in counts and its coloured versions in radial and azimuthal velocities.
- A secondary branch of the phase spiral at large positive  $V_Z$ , which is also detected but marginally in the counts projection. This is observed in the local phase spiral (see also A18 and Laporte et al. 2019) but also at angular momentum between angular momentum 1800 and 2400 km s<sup>-1</sup>kpc. This

branch seems to merge with the well-defined main phase spiral moving towards the outer Galaxy. A somehow similar branching is seen in the simulations by Hunt et al. (2021) (their figure 5). This secondary branch might be caused by complex phase mixing process (e.g. different groups of actions, steaming from non-uniform initial conditions, or with strong dependence on the position of the disc) or different perturbations.

- Different morphology of the phase spiral when splitting by angular momentum, including the expected flattening with  $Z$  at larger  $|L_Z|$  (also seen in DR2, e.g. Laporte et al. 2019, Bland-Hawthorn et al. 2019) but also trends departing from this expected flattening in a usual MW gravitational potential. While part of these trends could be due to selection effects (Appendix D), an easier explanation is our too simplistic modeling of the phenomena involved (see below).
- Differences in the spiral in counts and coloured by  $V_R$  at certain angular momentum. As seen in the simulations in Bland-Hawthorn & Tepper-García (2021) for an impact with a galactic satellite, the vertical projection coloured by  $V_R$  could be showing the combination of: 1) the density wave induced after a perturbation (mostly a density two-armed spiral structure in the impulsive and distant impact conditions, Toomre & Toomre 1972; Struck et al. 2011) that is linked to a  $L_Z$ - $V_R$  wave (Antoja et al. 2022), and 2) the vertical waves induced after the same perturbation. However, the exact way in which the planar and vertical disturbances are coupled is not yet well understood. Joining simple modelling of satellite perturbations such as the one in Gandhi et al. (2022) (vertical) and Antoja et al. (2022) (planar) could help in this. Exploring more complex models with enough resolution such as in Hunt et al. (2022) is also necessary.
- Mild changes of the phase spiral at different azimuth. These can be up to  $-0.006$  kpc/deg but these changes are not uniform (i.e. depend on the turn of the phase spiral).

Finally, we have estimated the phase mixing times from the phase spiral for the first time using data at different angular momentum and we find that:

- There is large variation with the times derived from measurements of the phase spiral at different height (different turns) and at different angular momentum: we see an increase of time with  $|L_Z|$  and especially with  $|Z|$ . The time differences can be of 0.7 Gyr using a single phase spiral at the angular momentum close to the Sun's one but different turns of the phase spiral (i.e. different  $Z$ ) and of 0.4 Gyr considering different angular momentum.
- The average time is of 0.5 Gyr. However, for 80% of our determinations we find times in the range of 0.3-0.9 Gyr.
- We find slightly larger times when using the B08 model (0.4-1. Gyr), systematically larger times for hotter orbits (0.4-1. Gyr) and smaller times for a re-scaled version of MW2014 (0.3-0.7 Gyr).
- The values obtained are very similar than the ones given in A18 which were 0.3-0.9 Gyr and are consistent in their upper limits with the determinations from the frequency of the wave  $L_Z$ - $V_R$  from Antoja et al. (2022). As in our original work A18, these times are consistent with the previous pericentre passage of Sagittarius.
- The mentioned trends with angular momentum and height are robust to using frequencies for hotter orbits, different potential models, different distance determinations, and possible (small) distance biases.

These variations are not expected for a signal that comes from the same phase mixing process. Recently, we found out that a simultaneous study (Frankel et al., submitted) also finds different time determinations at different angular momenta using action-angle variables. Below we discuss different explanations.

It could be that we are seeing the differences in the time of response to the perturbation of different disc regions. However, for the case of the Sagittarius impact in Gandhi et al. (2022) they found differences in the onset of the perturbation effects at different radius of the order of 100 Myr, which is smaller than what we measure. Besides, they do not see a clear trend with guiding radius. In addition the time differences with  $Z$  at a fixed angular momentum would hard to explain with this hypothesis alone. However, the spatial and temporal propagation of different bending waves remains poorly studied and we plan to examine this with various models in the future.

Another explanation is that there is a mismatch between the vertical and radial dependence of the potential in the models (that we used to compute the vertical frequencies) and in the real MW. Using this fact, one could actually infer the potential that could make these trends disappear. This is not trivial due to the degeneracy and the possible self-gravity effects.

Indeed, the time variations could also be evidence for self-gravity acting differently in different parts of the disc. Self-gravity tends to amplify the phase mixing times (Darling & Widrow 2019) and in particular could be of less importance in the outer parts of the disc (e.g. Shen & Sellwood 2006). This could mean that the times that we obtain in the outer parts, that is the larger times, are closer to the true perturbation time. However, the radial behaviour of different kind of bending waves that originate from different perturbations might be different (e.g. bending waves associated to the bar or due to external torques from galactic satellites or even from a misaligned halo) and has not been deeply studied.

Finally, our finding could be related to other aspects of the disc dynamics and how they interact with each other. By this we mean the effects of the bar, the spiral arms, the warp, and different bending and breathing modes, that could have acted or be acting in addition the vertical perturbation causing the phase spiral. For instance, Widmark et al. (2022) recently showed that some features of the vertical density and velocity seem related to the local spiral arm, while theoretical work have identified vertical velocity effects in spiral arm models (e.g. Faure et al. 2014; Kumar et al. 2022). In addition, if the disc midplane oscillates due to one of these additional distinct phenomena, the  $Z$ - $V_Z$  centroid of the phase spiral would oscillate and affect the time determinations.

To conclude, we see now more complexity in the morphology of the vertical projection and unexpected trends, possibly indicating, different perturbations (perhaps from different agents or different times), as already pointed out by Hunt et al. (2022) -after the discovery of the double phase spirals- and/or complex phase mixing processes. The variations of our derived phase mixing times with vertical position and angular momentum likely indicate too poor modelling due to uncertainties in the potential model for the Galaxy, neglecting self-gravity, existence/interaction of multiple perturbations or combinations of these. Although the new *Gaia* DR3 data definitively brings us a clearer picture of the MW phase spirals, there is still much to be understood and modelled.

*Acknowledgements.* Project supported by a 2021 Leonardo Grant for Researchers and Cultural Creators, BBVA Foundation. . The BBVA Foundation accepts no responsibility for the opinions, statements and contents included in the project and/or the results thereof, which are entirely

the responsibility of the authors. TA acknowledges the grant RYC2018-025968-I funded by MCIN/AEI/10.13039/501100011033 and by “ESF Investing in your future”. This work was (partially) funded by the Spanish MICIN/AEI/10.13039/501100011033 and by “ERDF A way of making Europe” by the “European Union” through grant RTI2018-095076-B-C21, and the Institute of Cosmos Sciences University of Barcelona (ICCUB, Unidad de Excelencia ‘María de Maeztu’) through grant CEX2019-000918-M. MB received funding from the University of Barcelona’s official doctoral program for the development of a R+D+i project under the PREDOCS-UB grant. CL acknowledges funding from the European Research Council (ERC) under the European Union’s Horizon 2020 research and innovation programme (grant agreement No. 852839). This work has made use of data from the European Space Agency (ESA) mission *Gaia* (<https://www.cosmos.esa.int/gaia>), processed by the *Gaia* Data Processing and Analysis Consortium (DPAC, <https://www.cosmos.esa.int/web/gaia/dpac/consortium>). Funding for the DPAC has been provided by national institutions, in particular the institutions participating in the *Gaia* Multilateral Agreement.

## References

- Anders, F., Khalatyan, A., Queiroz, A. B. A., et al. 2022, *A&A*, 658, A91
- Antoja, T., Helmi, A., Romero-Gómez, M., et al. 2018, *Nature*, 561, 360
- Antoja, T., Mateu, C., Aguilar, L., et al. 2015, *MNRAS*, 453, 541
- Antoja, T., Ramos, P., López-Guitart, F., Anders, F., Bernet, M., & Laporte, C. 2022, arXiv e-prints, arXiv:2206.03495
- Bailer-Jones, C. A. L. 2015, *PASP*, 127, 994
- Bailer-Jones, C. A. L., Rybizki, J., Fouesneau, M., Demleitner, M., & Andrae, R. 2021, *AJ*, 161, 147
- Bennett, M. & Bovy, J. 2019, *MNRAS*, 482, 1417
- Binney, J. & Schönrich, R. 2018, *MNRAS*, 481, 1501
- Binney, J. & Tremaine, S. 2008, *Galactic Dynamics: Second Edition*
- Bland-Hawthorn, J. & Gerhard, O. 2016, *ARA&A*, 54, 529
- Bland-Hawthorn, J., Sharma, S., Tepper-García, T., et al. 2019, *MNRAS*, 486, 1167
- Bland-Hawthorn, J. & Tepper-García, T. 2021, *MNRAS*, 504, 3168
- Blomme, R., Fremat, Y., Sartoretti, P., et al. 2022, arXiv e-prints, arXiv:2206.05486
- Bovy, J. 2015, *ApJS*, 216, 29
- Chequers, M. H., Widrow, L. M., & Darling, K. 2018, *MNRAS*, 480, 4244
- Chrobáková, Ž., López-Corredoira, M., Sylos Labini, F., Wang, H. F., & Nagy, R. 2020, *A&A*, 642, A95
- Cooley, J. W. & Tukey, J. W. 1965, *Math. Comp.*, 19, 297
- Darling, K. & Widrow, L. M. 2019, *MNRAS*, 484, 1050
- Faure, C., Siebert, A., & Famaey, B. 2014, *MNRAS*, 440, 2564
- Friske, J. K. S. & Schönrich, R. 2019, *MNRAS*, 490, 5414
- Gaia Collaboration, Brown, A. G. A., Vallenari, A., et al. 2018, *A&A*, 616, A1
- Gaia Collaboration, Drimmel, R., Romero-Gomez, M., et al. 2022a, arXiv e-prints, arXiv:2206.06207
- Gaia Collaboration, Prusti, T., de Bruijne, J. H. J., et al. 2016, *A&A*, 595, A1
- Gaia Collaboration, Recio-Blanco, A., Kordopatis, G., et al. 2022b, arXiv e-prints, arXiv:2206.05534
- Gaia Collaboration, Vallenari, A., Brown, A. G. A., et al. 2022c, arXiv e-prints, arXiv:2208.00211
- Gandhi, S. S., Johnston, K. V., Hunt, J. A. S., et al. 2022, *ApJ*, 928, 80
- García-Conde, B., Roca-Fàbrega, S., Antoja, T., Ramos, P., & Valenzuela, O. 2022, *MNRAS*, 510, 154
- Gravity Collaboration, Abuter, R., Aymar, N., et al. 2022, *A&A*, 657, L12
- Haines, T., D’Onghia, E., Famaey, B., Laporte, C., & Hernquist, L. 2019, *ApJ*, 879, L15
- Hunt, J. A. S., Price-Whelan, A. M., Johnston, K. V., & Darragh-Ford, E. 2022, arXiv e-prints, arXiv:2206.06125
- Hunt, J. A. S., Stelea, I. A., Johnston, K. V., et al. 2021, *MNRAS*, 508, 1459
- Katz, D., Sartoretti, P., Guerrier, A., et al. 2022, arXiv e-prints, arXiv:2206.05902
- Khoperskov, S., Di Matteo, P., Gerhard, O., et al. 2019, *A&A*, 622, L6
- Kumar, A., Ghosh, S., Kataria, S. K., Das, M., & Debattista, V. P. 2022, *MNRAS*, 516, 1114
- Laporte, C. F. P., Johnston, K. V., Gómez, F. A., Garavito-Camargo, N., & Besla, G. 2018, *MNRAS*, 481, 286
- Laporte, C. F. P., Minchev, I., Johnston, K. V., & Gómez, F. A. 2019, *MNRAS*, 485, 3134
- Li, Z.-Y. 2021, *ApJ*, 911, 107
- Li, Z.-Y. & Shen, J. 2020, *ApJ*, 890, 85
- Luri, X., Brown, A. G. A., Sarro, L. M., et al. 2018, *A&A*, 616, A9
- McMillan, P. J. 2017, *MNRAS*, 465, 76
- Mor, R., Robin, A. C., Figueras, F., Roca-Fàbrega, S., & Luri, X. 2019, *A&A*, 624, L1
- Purcell, C. W., Bullock, J. S., Tollerud, E. J., Rocha, M., & Chakrabarti, S. 2011, *Nature*, 477, 301
- Reid, M. J. & Brunthaler, A. 2020, *ApJ*, 892, 39
- Ruiz-Lara, T., Gallart, C., Bernard, E. J., & Cassisi, S. 2020, *Nature Astronomy*, 4, 965
- Rybizki, J., Green, G. M., Rix, H.-W., et al. 2022, *MNRAS*, 510, 2597
- Shen, J. & Sellwood, J. A. 2006, *MNRAS*, 370, 2
- Struck, C., Dobbs, C. L., & Hwang, J.-S. 2011, *MNRAS*, 414, 2498
- Tian, H.-J., Liu, C., Wu, Y., Xiang, M.-S., & Zhang, Y. 2018, *ApJ*, 865, L19
- Toomre, A. & Toomre, J. 1972, *ApJ*, 178, 623
- van der Walt, S., Schönberger, J. L., Nunez-Iglesias, J., et al. 2014, *PeerJ*, 2, e453
- Vasiliev, E. 2019, *MNRAS*, 482, 1525
- Virtanen, P., Gommers, R., Oliphant, T. E., et al. 2020, *Nature Methods*, 17, 261
- Wang, C., Huang, Y., Yuan, H. B., et al. 2019, *ApJ*, 877, L7
- Widmark, A., de Salas, P. F., & Monari, G. 2021, *A&A*, 646, A67
- Widmark, A., Widrow, L. M., & Naik, A. 2022, arXiv e-prints, arXiv:2207.03492
- Widrow, L. M., Gardner, S., Yanny, B., Dodelson, S., & Chen, H.-Y. 2012, *ApJ*, 750, L41
- Williams, M. E. K., Steinmetz, M., Binney, J., et al. 2013, *MNRAS*, 436, 101
- Younger, J. D., Besla, G., Cox, T. J., et al. 2008, *ApJ*, 676, L21

## Appendix A: Queries used to select samples

In this appendix we show a few examples of queries to the *Gaia* Archive <https://gea.esac.esa.int/archive/> to retrieve the data:

**Listing 1.** This query is used to retrieve stars with radial velocity with additional selection in temperature and RUWE (see main text) for our basic sample.

```
SELECT gaia.source_id, gaia.ra, gaia.dec,
gaia.parallax, gaia.pmra, gaia.pmdec,
gaia.radial_velocity, gaia.parallax_error,
gaia.phot_g_mean_mag, gaia.bp_rp,
gaia.grvs_mag, gaia.rv_template_teff
FROM gaiadr3.gaia_source AS gaia
WHERE gaia.radial_velocity is not null AND gaia.ruwe
< 1.4 AND gaia.rv_template_teff < 8500
```

**Listing 2.** This query is used to retrieve the fidelity flag (see main text) that is later merged by `source_id` with the data from query 1 for additional selection.

```
SELECT Rybizki.source_id, Rybizki.fidelity_v2
FROM external.gaiaedr3_spurious AS Rybizki
JOIN gaiadr3.gaia_source AS gaia ON gaia.source_id =
Rybizki.source_id
WHERE gaia.radial_velocity is not null
```

**Listing 3.** This query is used to retrieve the BJ distance (see main text) that is later merged by `source_id` with the data from query 1.

```
SELECT CBJ.source_id, CBJ.r_med_photgeo
FROM external.gaiaedr3_distance AS CBJ
JOIN gaiadr3.gaia_source AS gaia ON gaia.source_id =
CBJ.source_id
WHERE gaia.radial_velocity is not null
```

**Listing 4.** This query is used to retrieve the `source_id` of giants stars that is later merged by `source_id` with the data from query 1.

```
SELECT g.source_id
FROM gaiadr3.gaia_source AS g
WHERE (g.teff_gspphot < 5500 and g.teff_gspphot > 3000)
and (g.logg_gspphot < 3.) and (g.radial_velocity is not
null)
```

## Appendix B: Different distances

Here we compare the SH and the BJ distances of the 25 385 209 stars that remain after the cuts specified in Sect. 2. This is shown in Fig. B.1. On average, there is a negligible bias between distances. For example the relative differences are of 0.8% at around 1.5 kpc and of -0.9% at 4 kpc, that is smaller than 1% for the distances we are dealing with. For the 80% of stars the differences are smaller than 11% up to 4 kpc. Indeed when we calculate our  $Z_c$  using the different distance sets, our values barely change (Fig. B.2) and, consequently, our derived times do not change either (Fig. 12).

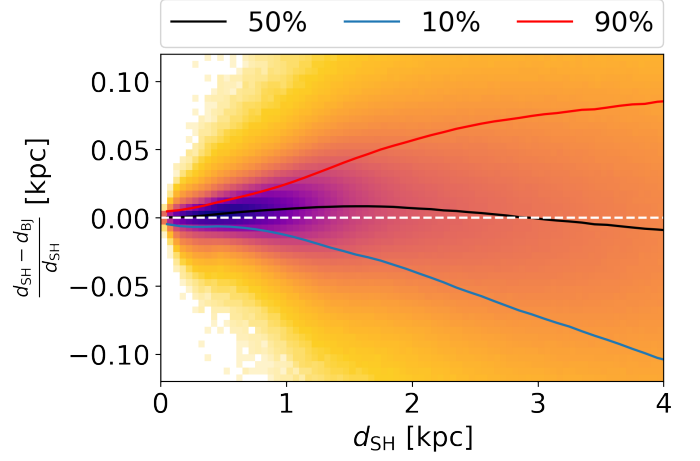


**Fig. B.1.** Comparison between sets of distances. Relative differences between distances from SH (Anders et al. 2022) and BJ distances (Bailer-Jones et al. 2021) as a function of SH distances for the stars in our sample that have these two distances available. The black line shows the median of the distribution, while the blue and red lower and upper lines show the 10 and 90 percentiles (i.e. they enclose 80% of stars).

## Appendix C: Effect of distance bias on the parameters of the phase spiral

Given that  $Z$  and  $V_z$  can be written as,

$$Z = d \sin(b) \text{ and} \quad (\text{C.1})$$

$$V_z = \kappa d \mu_b \cos(b) + V_{los} \sin(b), \quad (\text{C.2})$$

we can make some back-of-the-envelope manipulation to understand how the distances affect the shape of the phase space spiral.

Assuming that the effect of the distance bias only manifests at a certain distance, and that the range in Galactic latitude for disc stars shrinks with said distance, we can neglect the contribution of the line of sight velocity to  $V_z$  without loss of generality. We can further assume that the errors in the sky position are negligible, and that proper motion errors are perfectly Gaussian. If we do so, it is trivial to prove that, on average,

$$Z \simeq Z^{true} \frac{d}{d^{true}} \quad (\text{C.3})$$

and, similarly,

$$V_z \simeq V_z^{true} \frac{d}{d^{true}}. \quad (\text{C.4})$$

This result implies that both coordinates will suffer from a bias in the distance in a similar manner, at any position in the disc. For instance, if the distances are underestimated by 10%, the phase space spiral will shrink by the same amount, thus keeping the proportions. We note, however, that even if proportions are kept, the pitch angle will change and become larger if the spiral shrinks, and smaller if the spiral grows.

In general, we know that the bias increases with distance for most distance estimators based fully, or even partially, on the parallax. Therefore, the amount by which the spiral shrinks or grows will change as a function of  $Z$  for a certain  $X$  and  $Y$ , as the

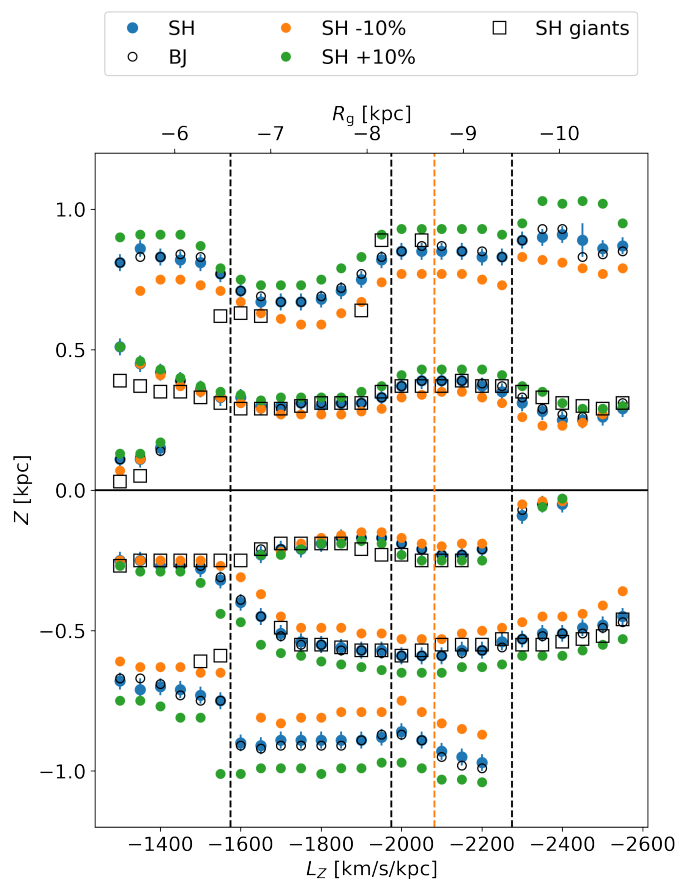


**Fig. B.2.** Crossing positions of the phase spiral for different distances. The blue circles and error bars mark the  $Z$  coordinate for  $V_z = 0$  ( $Z_c$ ) of the phase spiral determined from the edge detector for the SH sample. The other symbols indicate the crossings for the BJ distances and for distance biases of  $\pm 10\%$ .

heliocentric distance will increase with  $Z$ . Therefore, the deformation will not be as simple as a scaling of the original one.

Moreover, the process of estimating a distance from a parallax for one star usually leads to a probability distribution of distances that is not symmetric. Therefore, rather than having a simple bias, normally the mode of the resulting distance probability distribution is smaller than the true distance (which should coincide with the median), causing in turn a long tail towards big distances (Luri et al. 2018). This further complicates any attempt to predict how the phase spiral will look like.

To test these deductions, first we generate particles along a perfect Archimedean spiral in a manner such that the number of particles increases with the distance from the centre, which we do simply for visualisation purposes<sup>3</sup>. Once we have this *true* spiral, we place it at a certain heliocentric distance of our choice (this is the distance of the particles at  $Z=0$ ), and then calculate the true distance of all the particles in it by inverting Eqs. C.1 and C.2. Then, we draw a parallax for each particle from a normal distribution centred at its true parallax (inverse of its true distance), with an error set to a certain parallax over error.

<sup>3</sup> The area covered by a constant angular step increases along the spiral, as the distance from the centre grows, which causes the consequent drop in density we try to counteract by drawing the angles of the particles along the spiral from a Beta probability distribution function with  $a=2$  and  $b=5$ . In other words, the angles along the spiral are not drawn uniformly.

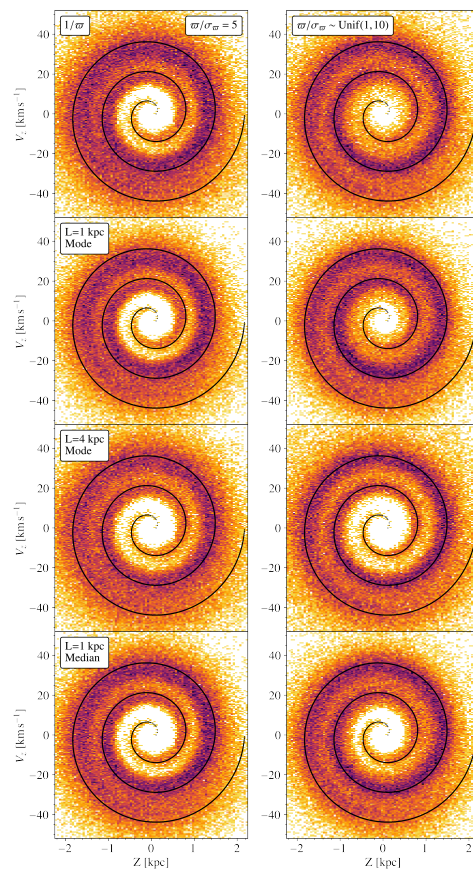


**Fig. C.1.** Effects of the distance bias on a perfect Archimedean spiral. For all panels, the centre of the spiral is at 4 kpc from the Sun, and the black curve is the true spiral. Left column: mock particles sampled with a constant parallax over error of 5. Right column: same but the parallax over error is sampled uniformly from 1 to 10. Rows correspond to different distances estimates, from top to bottom: parallax inversion, Bayesian estimate with  $L=1$  kpc and taking the mode of the posterior, same as above but with  $L=4$  kpc, Bayesian estimate with  $L=1$  kpc but taking the median of the posterior.

The left column of Fig. C.1 shows the effects of assuming a fixed parallax over error of 5 for all particles on a spiral that is located at 4 kpc from the Sun. The different rows correspond to different distances estimates: inverting the parallax or using the Bailer-Jones (2015) exponentially decreasing volume prior with different parameters. As we can see, the peak of the density is displaced inwards as expected (see above), with a long tail outwards accompanying it that blurs the signal. The right column of Fig. C.1 is similar to the left column, but now we have sampled the parallax over error randomly in the range 1 to 10. This results in a less biased spiral and slightly more blurred. The differences between models here is almost unnoticeable, although using the median instead of the mode of the posterior seems to provide some robustness in front of samples with different parallax over error. In general, though, we will have a mix of populations that depends on the location with respect to the Sun of the bin we are sampling, that is on the magnitude and colour distribution of the stars in that sub-sample and their heliocentric distances. And so, even if we cannot quantify the exact deformation of the spiral, it seems reasonable to expect it to shrink.

As a second test, we now recompute the phase space coordinates of the full sample after enlarging and decreasing their distances by 10%. These two new dummy samples help us, to begin with, to confirm that the approximations presented in Eqs.

C.3 and C.4 are, in general, valid. More importantly, with the new sample we can redo all calculations of our analysis. First in Fig. B.2 we show the  $Z_c$  of the phase spiral when distances are decreased by 10% (orange circles) and increased by 10% (green) which can be compared to the not-scaled SH distances (blue circles). In general we find that, the bias mostly reproduces our expectations, that is the  $Z_c$  are scaled by  $\pm 10\%$ . Some points differ from these expectations, which might be due to selection effects. In Fig. 12 we recomputed the phase mixing times for these new  $Z_c$  and we find that in most of the cases they fall within the errors of the standard case in 80% of the cases. More details are given in the main text. We note that although the biased  $Z_c$  do not fall within the errors of the standard  $Z_c$ , this is not the case for the time determinations. This is because to compute a time and its error bar, we use two consecutive  $Z_c$  and combine the different upper and lower limits of these two  $Z_c$  to obtain the minimum and maximum frequency differences that give place to the maximum and minimum times, respectively.

## Appendix D: Selection effects

In this appendix we examine the possible effects of the selection function of our samples in the determined  $Z_c$  and phase mixing times. The *Gaia* selection function is definitively a complicated matter. A possible worry for our work is that the characteristics of our sample, which certainly change with  $R$  and  $Z$ , bias our results. At different parts of the phase spiral and at different angular momentum the dominating population might change. For example, the proportion of thick disc over thin disc stars or the average age can vary with radius. In particular the average radial action of stars might change. We checked that, using actions computed in Gaia Collaboration et al. (2022b), mean values of the radial action in the  $L_Z$  and  $Z$  ranges explored here go from about 20 to 80  $\text{km s}^{-1}\text{kpc}$  (the 75 percentile can reach 120  $\text{km s}^{-1}\text{kpc}$ ). Here we found, however, that changing from  $J_R = 0$  to 200  $\text{km s}^{-1}\text{kpc}$  gave time differences mostly in the range of [0.04, 0.16] (Table 1), which is smaller than the systematic differences seen with angular momentum and height (Fig. 8). The trends of the derived times with angular momentum (and height) are hard to explain by only selection effects.

We nevertheless explore the mean value of different variables as a function of  $L_Z$  for the sample of stars with  $|\phi| < 20$  deg that is used in most of our analysis. This is shown in Figure D.1. Most of the quantities show a similar pattern (peak or valley at the the Sun's angular momentum, orange vertical dashed line) that is explained by having increasing distance for values of the  $|L_Z|$  departing from the Sun's one (right panel in the fifth row). It is not straightforward to translate this trends into trend in  $L_Z$  (or in  $Z$ ) since it is the difference between frequencies that enter in the calculation, but the peak/valley trends make the times increase with  $|L_Z|$  hard to explain. By contrast, the hypothesis given in our discussion (incorrectness of the potential models, neglecting self-gravity, etc) are easier and somehow expected causes.

In all panels of Figure D.1 we marked with vertical black dashed lines some positions of discontinuity in the  $Z_c$  ( $L_Z = -1575$  and  $-2275$   $\text{km s}^{-1}\text{kpc}$ , also marked in Fig. B.2) and in the time determinations ( $L_Z = -1975$   $\text{km s}^{-1}\text{kpc}$ ). Some of the lines could be correlated with jumps for example in the average magnitude of stars (two first panels of the first row, but with very small difference in magnitude) or with slight changes in the trends of colour (right panel in the first row). We also see some correlation with the known wave in  $VR$  (middle panel in the fourth row). At this point, thus, we cannot discard that the jumps are selection effects or real physical effects.

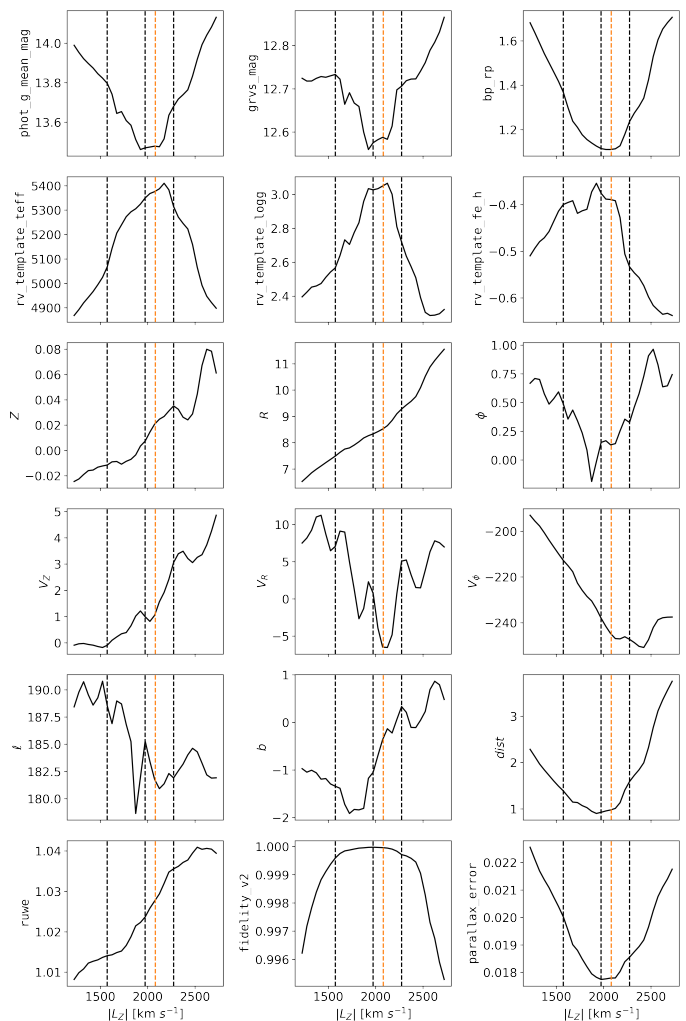


**Fig. D.1.** Investigation of some selection function effects. Mean values of different variables as a function of angular momentum  $L_Z$ . The dashed vertical lines indicate some positions where we see jumps in the shape of the phase spiral and/or the determined phase mixing times. The orange dashed line is the angular momentum of the Sun.

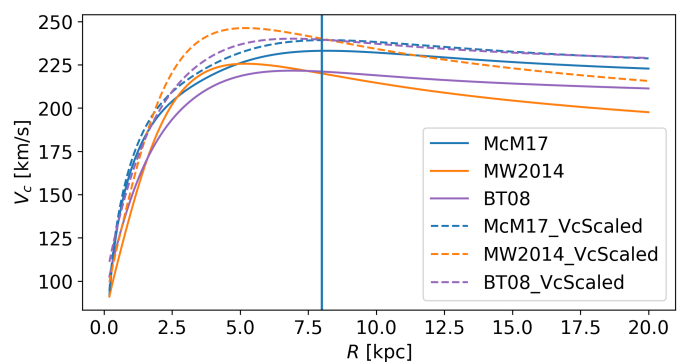


**Fig. E.1.** Circular velocity curves of the different potentials used.

## Appendix E: Additional material

Here we present the different gravitational potential models for the MW used in our study (Fig. E.1).